



**HAL**  
open science

## Clay platelet orientation inside self-standing beidellite clay films: Effect of silica nanospheres and link with macroscopic mechanical resistance

Sivagen Vydelingum, Pierre Levitz, Laurent J Michot, Thomas Bizien, Pierre Rabu, Ovidiu Ersen, Thibaud Chevalier, Natalie Malikova

### ► To cite this version:

Sivagen Vydelingum, Pierre Levitz, Laurent J Michot, Thomas Bizien, Pierre Rabu, et al.. Clay platelet orientation inside self-standing beidellite clay films: Effect of silica nanospheres and link with macroscopic mechanical resistance. *Applied Clay Science*, 2023, 231, 10.1016/j.clay.2022.106740 . hal-03858072

**HAL Id: hal-03858072**

**<https://hal.science/hal-03858072v1>**

Submitted on 14 Dec 2022

**HAL** is a multi-disciplinary open access archive for the deposit and dissemination of scientific research documents, whether they are published or not. The documents may come from teaching and research institutions in France or abroad, or from public or private research centers.

L'archive ouverte pluridisciplinaire **HAL**, est destinée au dépôt et à la diffusion de documents scientifiques de niveau recherche, publiés ou non, émanant des établissements d'enseignement et de recherche français ou étrangers, des laboratoires publics ou privés.

1 **Clay platelet orientation inside self-standing beidellite clay films:**  
2 **effect of silica nanospheres and link with macroscopic mechanical**  
3 **resistance**

4  
5 Sivagen Vydelingum<sup>a, b, c</sup>, Pierre Levitz<sup>a</sup>, Laurent J. Michot<sup>a</sup>, Thomas Bizien<sup>d</sup>,  
6 Pierre Rabu<sup>b</sup>, Ovidiu Ersen<sup>b</sup>, Thibaud Chevalier<sup>c</sup> and Natalie Malikova<sup>a</sup>

7  
8 <sup>a</sup>PHENIX Laboratory, UMR 8234 CNRS, Sorbonne University, 75005, Paris, France

9 <sup>b</sup>IPCMS Laboratory, UMR 7504 CNRS, University of Strasbourg, 67200, Strasbourg, France

10 <sup>c</sup>IFP Energies nouvelles, 1 et 4 avenue de Bois-Préau, 92852 Rueil-Malmaison, France

11 <sup>d</sup>Synchrotron SOLEIL, l'Orme des Merisiers, 91190, Saint-Aubin, France

12  
13 Corresponding author(s):

14 [sivagen.vydelingum@sorbonne-universite.fr](mailto:sivagen.vydelingum@sorbonne-universite.fr); [natalie.malikova@sorbonne-universite.fr](mailto:natalie.malikova@sorbonne-universite.fr)

## 20 Highlights

- 21 • Self-standing films of clay platelets and nanospheres were produced.
- 22 • Platelet orientation in the films was investigated by SAXS.
- 23 • Clay ordering within films is favoured for small platelets.
- 24 • Sphere-clay interactions modulate the tensile strength of films.

25

26

27

28

29

30

31

32

33

34

35

36

37

38

## 39 Abstract

40 Clay minerals and silica are essential components of soil. Understanding the multi-scale  
41 structure of a simple model system formed of (negatively charged) beidellite clay nanoplatelets  
42 and silica nanospheres is a first step in understanding the complex structure of soil. Due to their  
43 strong shape anisotropy, clay nanoplatelets exhibit preferential orientation at the microscopic  
44 level, both in aqueous dispersions and in dry deposits. Adding spherical colloids into the system  
45 changes the clay platelet organisation. These changes are studied here for the case of self-  
46 standing clay films, using a small angle X-ray scattering (SAXS) beamline, equipped with a  
47 goniometer and a rotating device. We investigated orientation of clay nanoplatelets as a function  
48 of the nanoplatelet and nanosphere sizes, their surface charge and sphere/platelet number ratio.  
49 Two methodologies are developed to calculate the nanoplatelet order parameter  $\langle P_2 \rangle$ : (a)  
50 background contribution is subtracted from the azimuthal profile curve at a given wavevector  
51  $q$  and (b) isotropic contribution is subtracted directly at the level of the 2D SAXS images.  
52 Smaller clay nanoplatelets ( $\sim 200\text{nm}$  in lateral size) exhibit a better orientation than larger  
53 platelets ( $> \sim 300\text{nm}$ ). Adding small positively and negatively charged nanospheres (diameter  $\sim$   
54  $30\text{nm}$ ) destroys the high degree of orientation of small clay platelets. Large spheres (diameter  
55 similar to the nanoplatelet size,  $\sim 300\text{nm}$ ) destroy orientation for both types of clay platelets. A  
56 simple tensile strength setup allows to measure the breaking stress of the self-standing films to  
57 make the link between microscopic and macroscopic structure. Films of small clay platelets  
58 without spheres were mechanically the most resistant. Films with added positively charged  
59 spheres were stiffer than films with negatively charged spheres. The methodology presented  
60 here opens perspectives for the study of structure and mechanical response of clay deposits.

61 Keywords: clay nanoplatelets, silica nanospheres, self-standing films,  
62 SAXS, orientation, tensile strength

63

## 64 1. Introduction

65 Natural soils are complex multi-scale assemblies of inorganic, organic and biological  
66 components. The organization of the various soil components plays a major role in the  
67 functioning of the whole system and controls to a large extent the fertility, stability and  
68 degradation of soils. Among the various soil constituents, clay minerals are of prime importance  
69 and clay content is indeed a key factor in soil taxonomy (Soil Survey Staff. 1999). These  
70 minerals are layered materials with unique properties such as high surface area, water retention,  
71 ion exchange capacity and fixation of organic matter (Velde, 1992; Bergaya et al., 2006). Due  
72 to these properties, they play a major role in soil functioning and control to a large extent plant  
73 nutrition, water retention, transport and mechanical strength. This is directly related to the  
74 microstructure resulting from the association of clays with other soil components such as silts  
75 and sands. This generates various assemblies that have been studied extensively (e.g. Stoops  
76 and Jongerius, 1975; Fiès and Stengel, 1984; Bruand and Prost, 1987, 1988; Bruand et al.,  
77 1988.; Attou et al., 1998; Rozenbaum et al., 2012). In that context, developing a model system  
78 mimicking the association of silts and clays could provide relevant information on the pertinent  
79 parameters affecting microstructure by analyzing in detail the multi-scale organization of these  
80 two components in the solid state.

81 The model system investigated is composed of size-sorted Na-exchanged beidellite clay  
82 particles (the swelling component of soil) and silica spheres (the silts). The behavior of aqueous  
83 suspensions of beidellite platelets has been studied in detail (Paineau et al., 2009, 2011) and  
84 reveals the existence of an Isotropic/Nematic phase transition occurring before the sol/gel

85 transition. These features are slightly modified upon addition of colloidal spheres(Hilhorst et  
86 al., 2014; Landman et al., 2014; Bailey et al., 2015), which reveals the presence of interactions  
87 between both components in the system. For an equivalent system with gibbsite platelets and  
88 silica nanospheres enhanced density fluctuations were observed (Doshi et al., 2011). However,  
89 how these interactions affect the structure of films formed from these colloidal mixtures  
90 remains to be analyzed. To shed new light on this issue, in the present work we varied the size  
91 of both clay nanoplatelets and silica nanospheres, as well as the relative proportions of both  
92 components. In addition, for modifying the interactions in the mix, as clay particles are  
93 negatively charged (Bergaya et al., 2006) we used classical silica spheres that are negatively  
94 charged at neutral pH, and alumina coated silica spheres that display an isoelectric point around  
95 8 and can then be positively charged for lower pH values.

96 In this manuscript we focus on the effect of nanosphere component on the orientational  
97 features of clay nanoplatelets in composite self-standing films, which may be relevant in the  
98 context of soil degradation by crusting. In a very recent study the orientation of clay phases in  
99 real soil samples was investigated using synchrotron-based microdiffraction experiments and it  
100 was shown that the presence of coarse quartz grains had a significant effect on clay orientation  
101 in the crusts (Geoffroy et al., 2022). In our approach, we developed a rotating device in order  
102 to analyze in detail, using SAXS, the evolution of clay anisotropy in dry self-standing films  
103 formed with various ratios of different spheres and platelets. Using a recently developed  
104 orientation distribution function (ODF) (Dabat et al., 2019, 2020), we examine how the various  
105 parameters of the initial suspension affect the orientation of clay platelets in the film. Indeed,  
106 even if Maier-Saupe ODF is usually used for platelet system, it is not able to fit experimental  
107 data for clay systems at low and high order parameter values (Dabat et al., 2019). The new  
108 generalized ODF for clay systems is able to fit the whole range of order parameter. In parallel,  
109 using a recently developed tensile strength setup (Carrier et al., 2016,) we examine the potential

110 relationships between clay orientation in the films extracted from SAXS measurements and  
111 mechanical strength of the film at the macroscopic scale.

## 112 2. Materials and methods

### 113 2.1 Sample preparation

#### 114 2.1.1 Clay size sorting and purification

115 Beidellite SBId-1 from Idaho with an average structural formula that can be written as  
116  $(\text{Si}_{7.27}\text{Al}_{0.73})(\text{Al}_{3.77}\text{Fe}_{0.11}^{3+}\text{Mg}_{0.21})\text{O}_{20}(\text{OH})_4\text{Na}_{0.67}$  ) was purchased from the Source Clays  
117 Minerals Repository of Clay Minerals Society (Purdue University). Prior to use, beidellite  
118 natural clay was sodium exchanged, purified and size sorted according to previously established  
119 procedures (Michot et al., 2004; Paineau et al., 2011). Table 1 presents the size and charge  
120 characteristics of the two sizes of beidellite used in the present study (Paineau et al., 2011).

121 **Table.1:** Beidellite platelet characteristics: Average lateral size, average thickness,  
122 polydispersity and CEC.

Size fraction	S1	S3
Lateral size (nm)	330	210
Polydispersity diameter (%)	47	38
CEC (meq/100g)	64.2	94.3

123

124 Thickness of size fraction S1 and S3 platelets is around 1 nm. Presence of kaolin particles  
125 in size fraction S1 explains a CEC value low as  $64.2 \text{ meq}/100\text{g}$ . Regarding S3 CEC slightly  
126 higher value than expected from structural formula is mostly due to the platelets small size and  
127 the charges of platelet edge taken into account in CEC value.

128

129 2.1.2 Silica spheres

130 Small silica spheres: ludox TM-50 was purchased from Sigma-Aldrich (30 nm in diameter)  
131 and ludox CL-P was purchased from Grace (28 nm in diameter). Large silica spheres: silica  
132 spheres were purchased from cospheric (CS) and from Creative diagnostics (CD) (both 300 nm  
133 in diameter). Both Ludox CL-P and CD spheres are coated by Al<sub>2</sub>O<sub>3</sub> and then bear a positive  
134 charge surface for pH values ≤ 6 (Supplementary info 1). The zeta potential of beidellite  
135 platelets is around -40 mV over the whole pH range (Housni et al., 2020). Ludox TM-50 and  
136 cospheric spheres were used at pH 8 and are then negatively charged whereas Ludox CL-P and  
137 CS were used at pH 4 where they bear a positive surface charge (Table 2). Charge densities for  
138 the different spheres are of similar value and only of opposite charge (Supplementary info 1).

139 **Table. 2:** Sphere characteristics: diameter, pH used for deposit and charge surface.

	Ludox TM-50	Ludox CL-P	Cospheric silica	CD silica
Diameter (nm)	30	28	300	300
pH used for deposit	8	4	8	4
Surface charge at pH used	(-)	(+)	(-)	(+)

140

141 2.1.3 Self-standing films

142 Aqueous suspensions of clay platelets and silica spheres are mixed to produce suspensions  
143 of different sphere/platelet nominal number ratios ( $R_n$ ) given by the following equation:

144 
$$R_n = \frac{N_s}{N_p} \quad (1)$$

145 Where  $N_s$  is the number of spheres and  $N_p$  the number of platelets per unit volume. Mixed  
146 sphere/platelet dispersions are deposited onto an aluminium cup and dried at room temperature  
147 to form self-standing films. Self-standing films of a few tenths of micrometers in thickness are



148 recovered. For large spheres, the number ratios used for small spheres do not yield self-standing  
149 films. Therefore, a surface ratio is used instead of a number ratio, according to:

$$150 \quad R_s = R_n \frac{8R^2}{d^2} \quad (2)$$

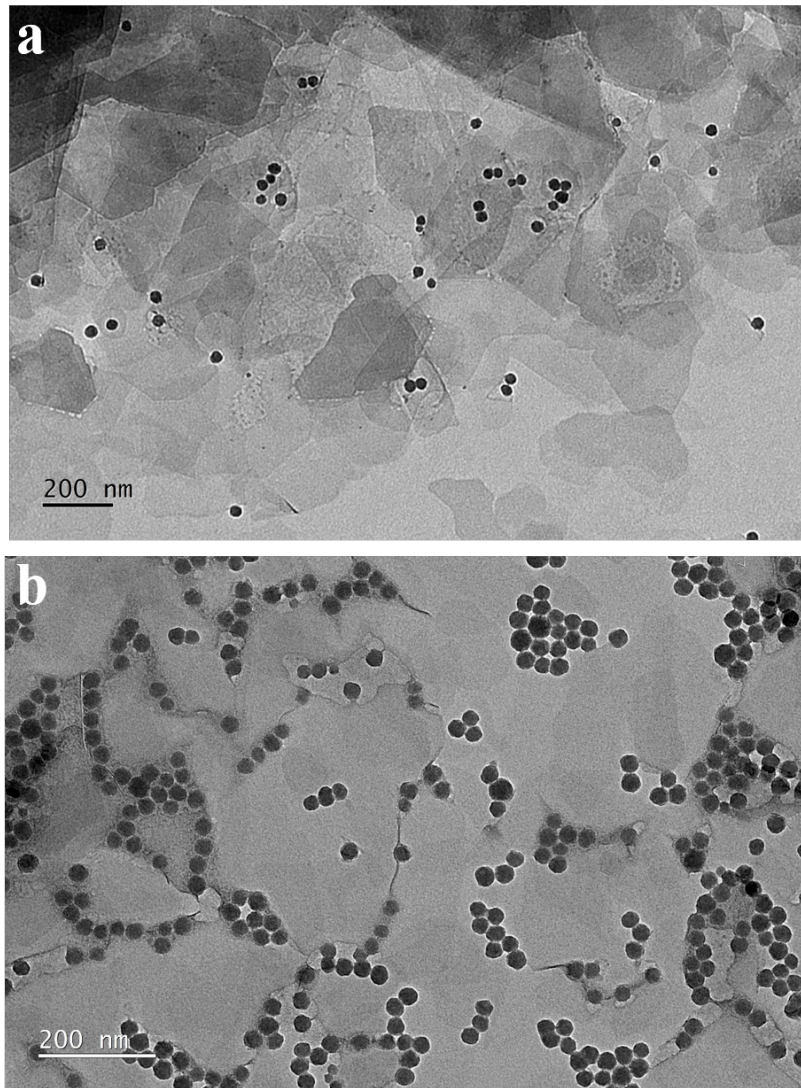
151 where  $d$  is the platelet lateral size and  $R$  the sphere radius. The sequence of films produced is  
152 summarized in Table 3. Number ratio  $R_n$  is chosen in order to understand sphere-platelet  
153 interactions by varying their relative number. Compared to this, the surface ratio  $R_s$  helps to  
154 estimate the number of platelets needed to cover the surface of a large sphere.

155 Figure 1 presents TEM images of mixed platelet-sphere deposits. To produce TEM compatible  
156 deposits (maximum thickness of 100nm), mixed suspensions of platelets and spheres at a  
157 required ratio were deposited on TEM grids and left to evaporate. Both spheres and platelets  
158 can be easily distinguished in the images. TEM image with positive spheres (Figure 1a) displays  
159 a relatively homogeneous mix of the two components and no phase separation. Most of the  
160 positive spheres are on the lateral surface of the platelets and only a few are close to platelet  
161 edges. Several layers of clay platelets can be seen on the image. The image with negative  
162 spheres (Figure 1b) presents areas of phase separation of the two components, spheres are  
163 located mainly on platelet edges. Figure 2 presents SEM images of the mixed self-standing  
164 films (a few tens of  $\mu\text{m}$  thick). S1 beidellite self-standing films without spheres (Figure. 2a)  
165 display a weaker clay platelet alignment compared to S3 beidellite films without spheres  
166 (Figure 2b). The clay platelet alignment is even weaker for composite films of S3 beidellite  
167 with large positively charged spheres (Figure 2c).

168 **Table. 3:** Number and surface ratios,  $R_n$  and  $R_s$ , used for small and large spheres to produce  
169 self-standing films.

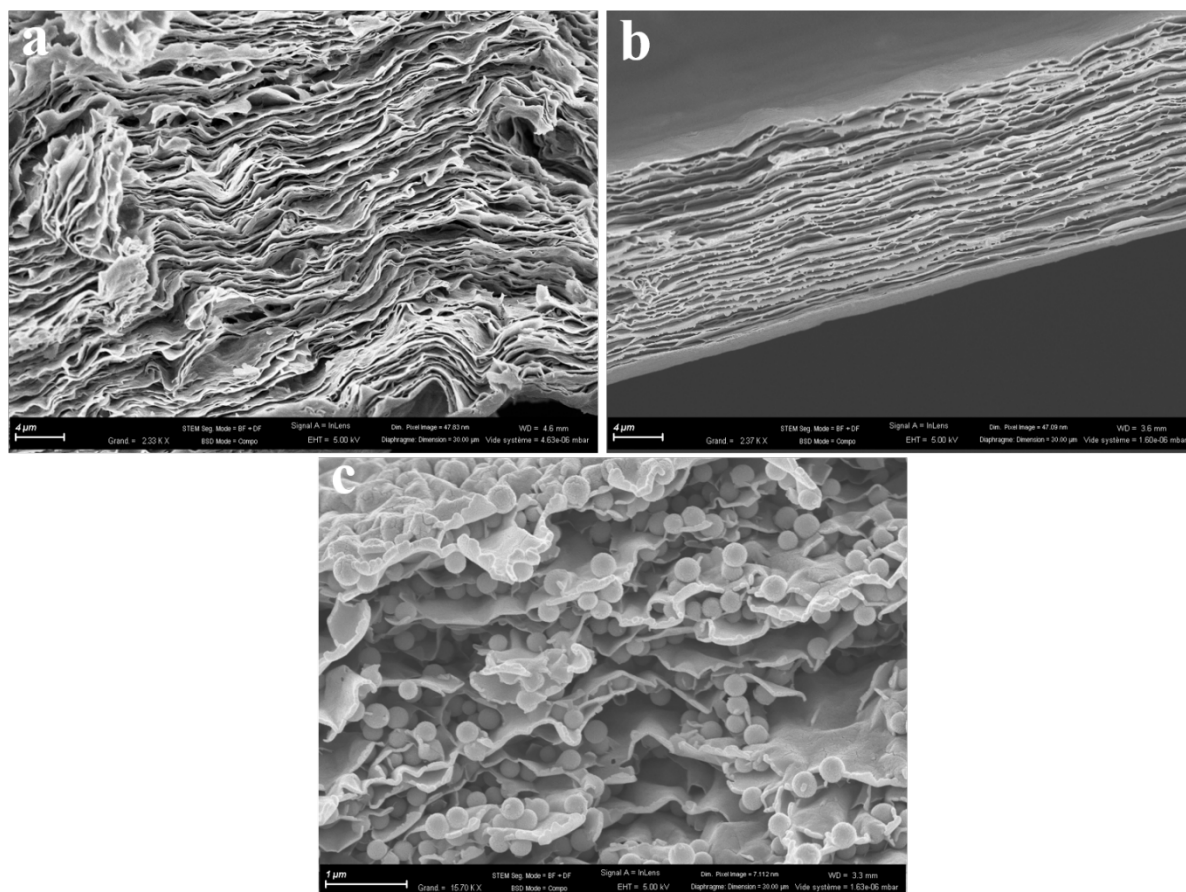
170

Deposits with small spheres $R_n$	Deposits with large spheres		
	$R_n$	$R_S$ equivalent (S1 platelets)	$R_S$ equivalent (S3 platelets)
0.3	0.002	0.003	0.009
1.0	0.005	0.008	0.022
3.0	0.016	0.026	0.072



172

173 **Figure. 1** : TEM images of beidellite clay platelets mixed with silica spheres. TEM projections  
 174 images at  $0^\circ$ . (a) S1 beidellite (lateral size 330 nm) mixed with ludox CL-P (positively charged  
 175 small spheres, diameter 28 nm) at  $R_n = 0.3$ . Image size: 4008x2642. (b) S3 beidellite (lateral  
 176 size 210 nm) mixed with ludox TM-50 (negatively charged small spheres, diameter 30 nm) at  
 177  $R_n = 2$ . Image size: 4008x2642.



178

179 **Figure. 2** : SEM images of self-standing films of beidellite clay platelets mixed with silica  
 180 spheres. (a) S1 beidellite (lateral size 330 nm) without spheres. (b) S3 beidellite (lateral size  
 181 210 nm) without spheres. (c) S3 beidellite mixed with CD silica (positively charged large  
 182 spheres, diameter 300 nm).

## 183 2.2 Small Angle X-ray Scattering

### 184 2.2.1 Beamline setup

185 SAXS experiments were conducted at SOLEIL synchrotron on beamline SWING at a fixed  
 186 energy of 12 keV, i.e. a fixed wavelength of  $1 \text{ \AA}$  and two sample-to-detector distances (0.5 m  
 187 and 6 m). Hence, the available  $q$  range varied from  $0.002 \text{ \AA}^{-1}$  to  $2 \text{ \AA}^{-1}$  ( $q = \frac{4\pi(\sin\theta)}{\lambda}$ , where  
 188  $2\theta$  is the scattering angle and  $\lambda$  the X-ray wavelength). 2D scattering signal was collected on  
 189 an Eiger 4M detector.

190 2.2.2 Goniometer and rotating device

191 A goniometer and a rotating device were installed onto the SAXS beamline. Using a razor,  
192 clay films were cut into slabs (an approximate shape of a rectangular cuboid, slab thickness of  
193 the order of 100  $\mu\text{m}$ , length of several mm). The slabs were glued to a needle's top  
194 (Supplementary info 2). The needle itself was glued to a small copper piece which was inserted  
195 into the goniometer head. The goniometer allowed adjusting the slab orientation in the vertical  
196 direction. The entire set-up (including the goniometer head) was then allowed to rotate and  
197 SAXS patterns were collected at different rotation angles, which enables defining properly  
198 sample orientation to determine the anisotropy of clay platelets inside the film (Figure 3).

199

200 2.3 Tensile strength measurement

201 A setup developed by (Carrier et al., 2016) was used to perform tensile strength  
202 measurements on self-standing films cut into a specific form to allow an equal load distribution  
203 on the film (Supplementary info 3). Breaking stress measurements were performed by gradually  
204 increasing the stress on the film (a bottle fixed by a thread to the setup was gradually filled with  
205 water). Film deformation was not investigated during the experiment. Breaking stress  $\sigma$  was  
206 estimated by the following equation:

207 
$$\sigma = \frac{mg}{S} \quad (3)$$

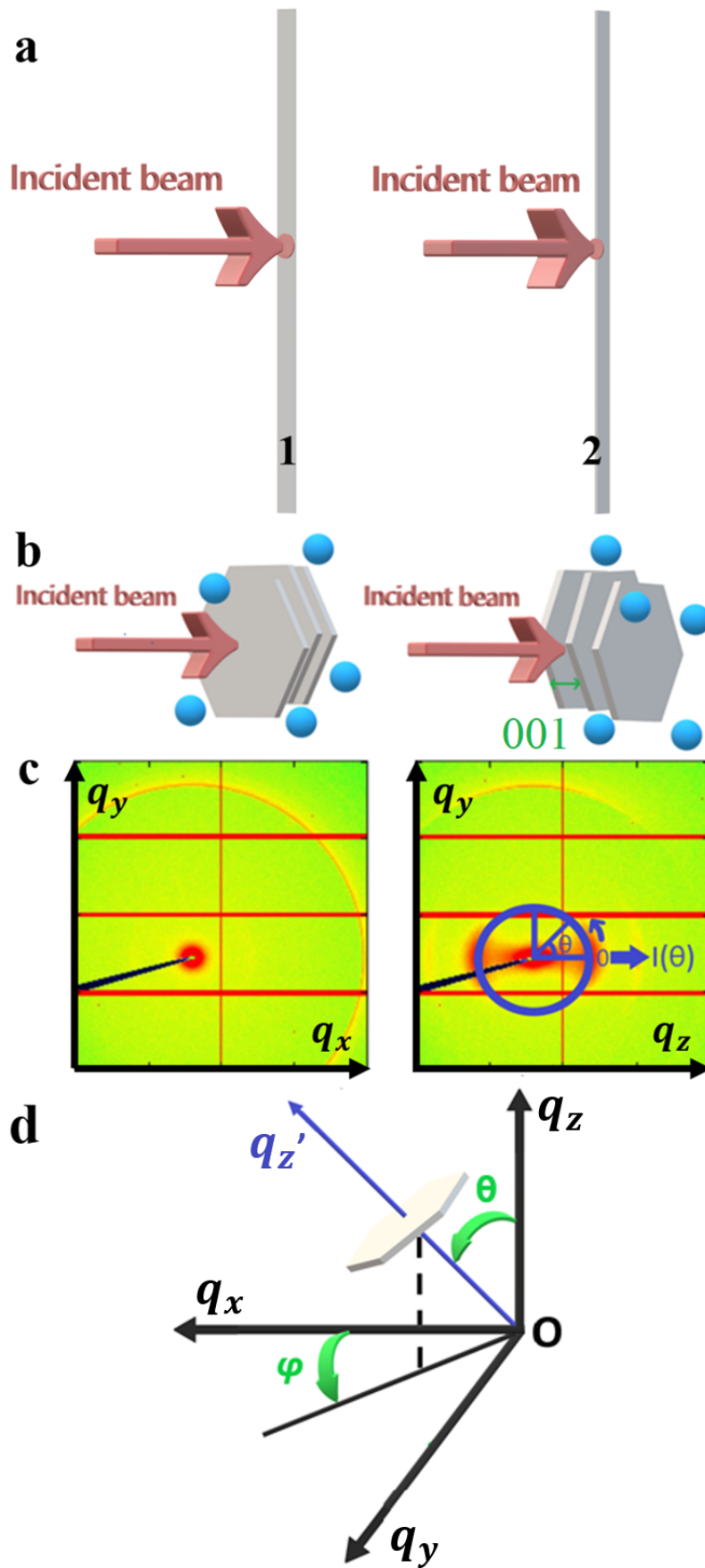
208 Where  $m$  corresponds to the mass of water present in the bottle necessary to split the film,  $S$  is  
209 the film's surface under stress. Tensile strength measurements were made in the following range  
210 of relative humidity ( $RH$ ) and temperature:  $RH = 20 - 24\%$ ,  $T = 19.4 - 21.6\text{ }^\circ\text{C}$ . As  
211 reported by (Carrier et al., 2016),  $RH$  has a significant influence on the mechanical resistance  
212 of self-standing films. In the present case, by working at constant  $RH$ , the differences in  
213 breaking stress can be assigned to changes in the film microstructure.

214           3 Results and Discussion

215           3.1 Methodology of SAXS data analysis

216           3.1.1 Sample orientation

217           Rotation of the film slab allowed to determine two specific clay film orientations (FACE  
218 and SIDE) and thus assess the clay platelet anisotropy inside the deposit (Figure 3a). In the  
219 FACE orientation, films of clay platelets and spheres feature only an isotropic 2D SAXS pattern  
220 (Figure 3b and Figure 3c left), while in the SIDE orientation, the 2D SAXS pattern reveals an  
221 anisotropic contribution originating in the 001 reflection of clay platelet stacking (Figure 3b  
222 and Figure 3c right). Intensity modulation  $I(\theta)$  was obtained from azimuthal signal variation  
223 in the SIDE position, at the 001 peak maximum ( $q = 0.5\text{\AA}^{-1}$ ) (Figure 3c right). The hk0  
224 reflection possesses an isotropic contribution in the FACE orientation of the films (Figure 3c  
225 left), whereas in the SIDE orientation hk0 contribution is anisotropic and is perpendicular to  
226 the 001 reflection (Figure 3c right).



228 **Figure. 3** : Sample under incident beam in SAXS experiment. (a) First sample position (FACE):  
 229 the incident beam arrives perpendicular to the “face” of the deposit. Second sample position  
 230 (SIDE): the incident beam arrives from the “side” of the deposit. (b) Schematic drawing of the  
 231 clay platelets and spheres in the FACE (left) and SIDE (right) sample position. Anisotropy of  
 232 platelet orientation and the 001 reflection (signature of platelet stacking) are observable in the  
 233 second (SIDE) position. (c) 2D SAXS patterns on the detector. Intensity modulation  $I(\theta)$  was  
 234 obtained from azimuthal signal variation in the SIDE position, at the 001 peak maximum ( $q =$   
 235  $0.5\text{\AA}^{-1}$ ). (d) Clay platelet orientation spherical coordinates in the reciprocal space  $(q_x, q_y, q_z)$  .

236

237 Clay platelets are a transverse isotropic system (Figure 3d) and the azimuthal profile  $I(\theta)$  in  
 238 the reciprocal space  $(q_x, q_y, q_z)$  allows to define and calculate an orientation distribution  
 239 function (ODF)  $f(\theta)$  (Dabat et al., 2019, 2020). The angle  $\varphi$  is chosen uniformly in  $(0, 2\pi)$ , this  
 240 range is found in uniaxial nematic phase. ODF features are described by the following equations  
 241 (Dabat et al., 2019, 2020):

$$242 \quad f(\theta) \geq 0 \quad (4)$$

$$243 \quad f(\theta) = f(\pi - \theta) \quad (5)$$

$$244 \quad \int_0^{\pi} f(\theta) \sin \theta d\theta = 1 \quad (6)$$

$$245 \quad f(\theta) = \frac{I(\theta)}{\int_0^{\pi} I(\theta) \sin \theta d\theta} \quad (7)$$

246 The order parameter  $\langle P_2 \rangle$  can then be defined for quantifying clay platelets orientation:

$$247 \quad \langle P_2 \rangle = \int_0^{\pi} \frac{1}{2} (3 \cos^2 \theta - 1) f(\theta) \sin(\theta) d\theta \quad (8)$$

248 This order parameter is commonly applied to nematic liquid crystal systems and is also referred  
 249 to as the nematic order parameter (Hermans and Platzek, 1939).  $\langle P_2 \rangle$  varies between  $-1/2$  and  
 250 1. Particles are randomly oriented when  $\langle P_2 \rangle = 0$  and perfectly aligned for  $\langle P_2 \rangle = 1$ .

251 Recently a new generalized ODF was developed by (Dabat et al., 2019) for clay phases. This  
252 function is based on maximum entropy minimisation and is described by the following  
253 equation:

$$254 \quad f(\theta) = k \exp \left[ \frac{\lambda}{2} (3 \cos^2(\theta - \Psi) - 1) + \frac{0.005\lambda^5}{8} (35 \cos^4(\theta - \Psi) - 30 \cos^2(\theta - \Psi) + 3) \right] \quad (9)$$

255 Where  $k$  is a normalization constant,  $\lambda$  the spreading of ODF and  $\Psi$  the deviation angle between  
256 detector azimuthal profile reference and ODF maximum. ODF model from eq. (9) was used to  
257 fit experimental data and estimate  $\langle P_2 \rangle$  value.

258 In order to isolate the  $\langle P_2 \rangle$  parameter corresponding to the clay platelet anisotropic  
259 contribution, two methodologies were developed to remove the underlying isotropic  
260 contribution (mostly due to scattering signal from the spheres). In the following, S1 beidellite  
261 mixed with ludox CL-P at  $R_n = 0.3$  is used as an example to explain the two methodologies.

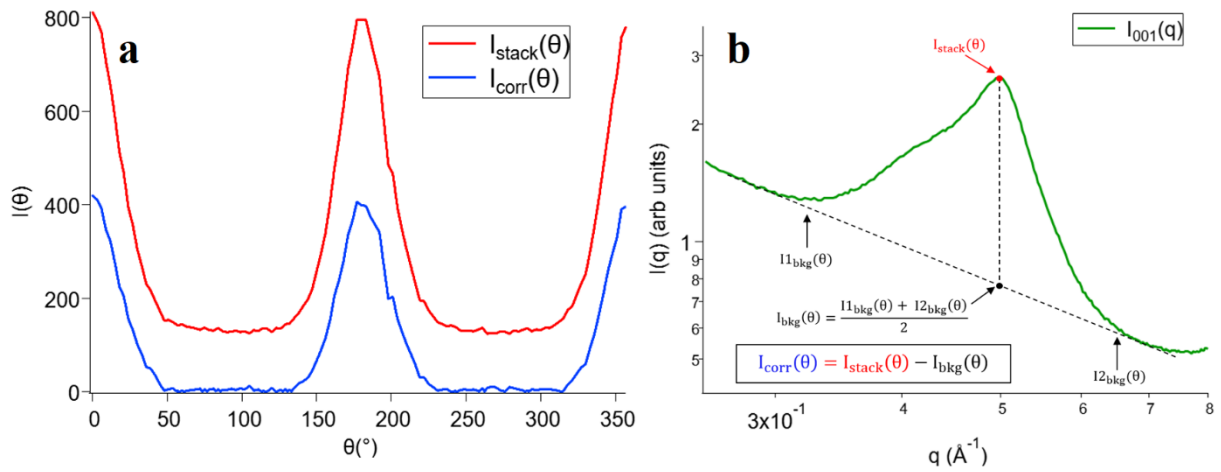
262

### 263 3.1.2 First methodology: background azimuthal profile subtraction

264 The first methodology used in this work was derived from (Dabat et al., 2020). All the  
265 azimuthal profiles were extracted from 2D SAXS patterns in the SIDE orientation, where clay  
266 platelet anisotropy is apparent (Figure 3c right). The azimuthal profiles of scattered intensity,  
267  $I(\theta)$ , necessary to obtain the corrected azimuthal profile used to determine  $\langle P_2 \rangle$  are represented  
268 in Figure 4a. The background  $I_{bkg}(\theta)$  contribution was estimated by averaging azimuthal  
269 profiles in the  $q$ -range  $0.3 - 0.4 \text{ \AA}^{-1}$  ( $I1_{bkg}(\theta)$ ) and  $0.6 - 0.7 \text{ \AA}^{-1}$  ( $I2_{bkg}(\theta)$ ) (Figure 4b).  
270 The mean contribution was then subtracted from  $I_{stack}(\theta)$  profile at the stacking peak  
271 maximum,  $q = 0.5 \text{ \AA}^{-1}$  (Figure 4b). The corrected  $I_{corr}(\theta)$  profile no longer exhibits non-zero  
272 contributions between  $60^\circ$ - $120^\circ$  and  $240^\circ$ - $300^\circ$  and thus contains scattered intensity only from



273 oriented clay platelets (Figure 4a and b). In the last step, ODF was derived from this corrected  
 274  $I_{corr}(\theta)$  profile using eq.(7) (Figure 6a).



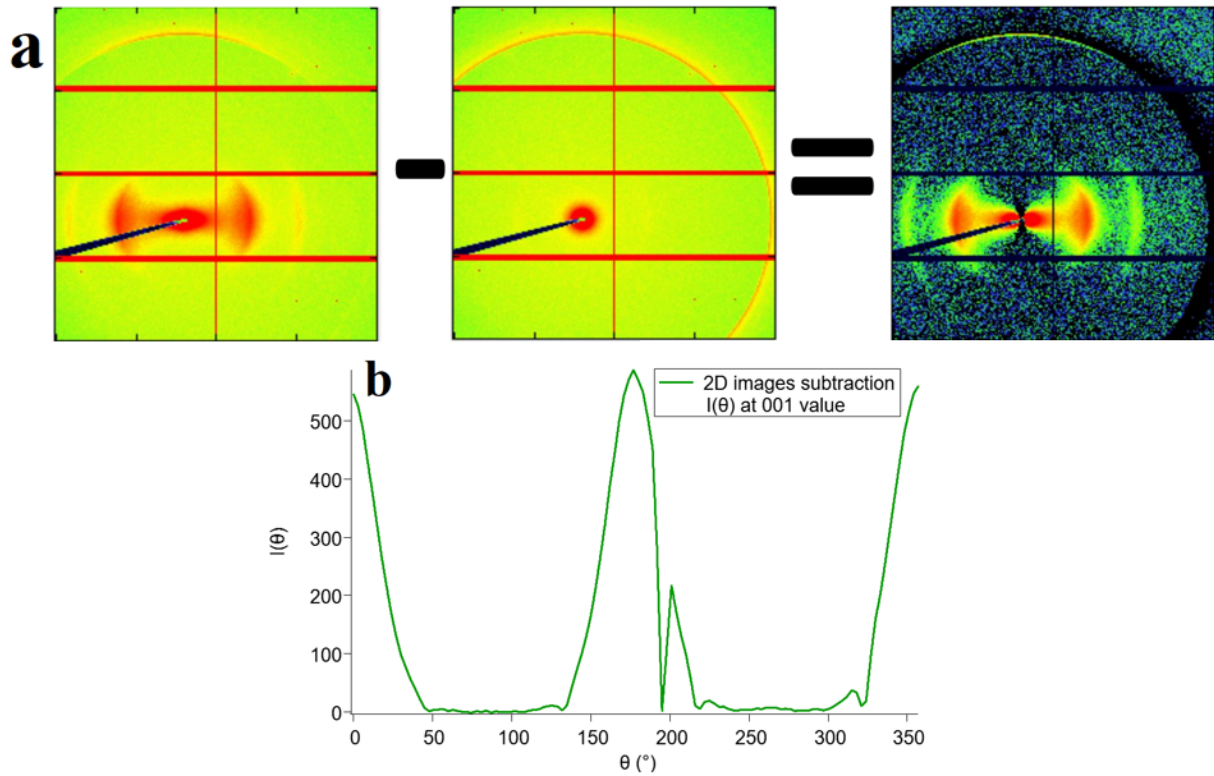
275  
 276 **Figure. 4** : First methodology based on isotropic azimuthal profile subtraction. Sample: S1  
 277 beidellite + ludox CL-P,  $R_n = 0.3$ . (a) (red curve)  $I_{stack}(\theta)$  at 001 value  $q = 0.5 \text{ \AA}^{-1}$ . (blue  
 278 curve) Obtained  $I_{corr}(\theta)$  after subtraction between background  $I_{bkg}(\theta)$  and  $I_{stack}(\theta)$  at 001.  
 279 (b) Calculation of background contribution on 001 peak  $I(q)$ .  $I_{1bkg}(\theta)$  is calculated between  
 280  $q = 0.3 - 0.4 \text{ \AA}^{-1}$  and  $I_{2bkg}(\theta)$  between  $q = 0.6 - 0.7 \text{ \AA}^{-1}$ . Background contribution  
 281  $I_{bkg}(\theta)$  is derived from  $I_{1bkg}(\theta)$  and  $I_{2bkg}(\theta)$  azimuthal profiles average. Obtained  $I(\theta)$  after  
 282 subtraction between mean  $I(\theta)$  and  $I(\theta)$  at 001.  $I_{stack}(\theta)$  is estimated at 001 maximum peak  
 283 value  $q = 0.5 \text{ \AA}^{-1}$ . The corrected  $I_{corr}(\theta)$  is the result of the background  $I_{bkg}(\theta)$  subtraction  
 284 to  $I_{stack}(\theta)$ .

285

### 286 3.1.3 Second methodology: 2D SAXS pattern subtraction

287 Second methodology was based directly on the 2D SAXS patterns acquired in the FACE  
 288 and SIDE sample orientations for a given sample (Figure 3c). The 2D SAXS pattern in the  
 289 FACE orientation was subtracted from the 2D SAXS pattern in the SIDE orientation (Figure  
 290 5a). The subtraction between orientations is correct due to the correction and normalization in  
 291 transmission of SAXS patterns. The resulting 2D SAXS pattern is presented in Figure 5a.  
 292 Azimuthal profile was then extracted at the 001-value  $q = 0.5 \text{ \AA}^{-1}$  in the subtracted 2D pattern.

293 Obtained intensity modulation  $I(\theta)$  provided only the anisotropic contribution, negligible  
 294 intensity between  $60^\circ$ - $120^\circ$  and  $240^\circ$ - $300^\circ$  was observed (Figure 5b). The corresponding ODF  
 295 is represented in Figure 5b.



296

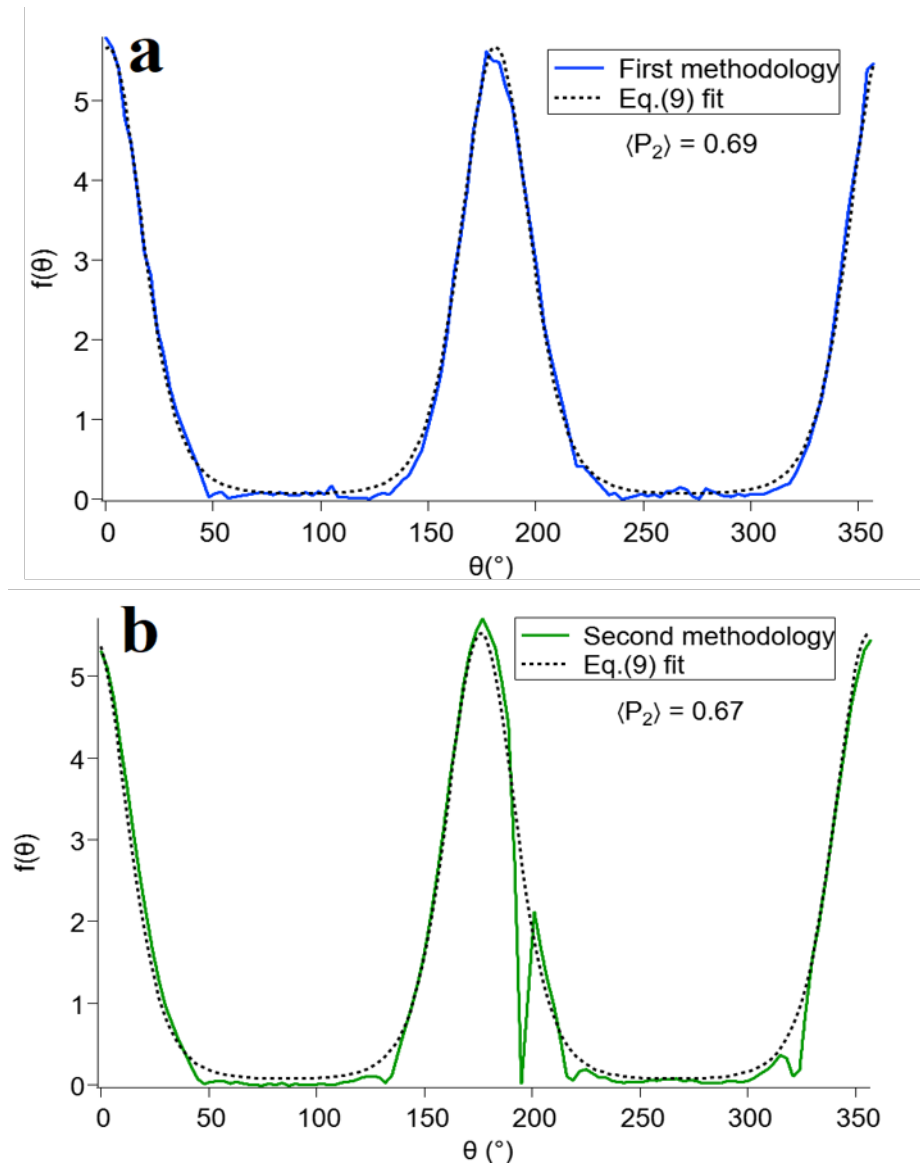
297 **Figure. 5** : Second methodology based on 2D SAXS pattern subtraction. Sample: S1 beidellite  
 298 + ludox CL-P,  $R_n = 0.3$ . (a) 2D SAXS patterns from the SIDE and FACE orientation (see  
 299 Figure 3): pattern for FACE orientation is subtracted from that of the SIDE orientation. (b)  
 300 Intensity modulation  $I(\theta)$  extracted at  $q = 0.5 \text{ \AA}^{-1}$  on the subtracted 2D pattern.

301

### 302 3.1.4 Fitting of ODF profiles and order parameters

303 The experimental ODFs resulting from the two above-mentioned methods are displayed  
 304 in Figure 6. Both ODFs were fitted with eq.(9) and  $\langle P_2 \rangle$  was calculated according to eq.(8). The  
 305 obtained results are almost equivalent as the  $\langle P_2 \rangle$  values derived by both methods only differ  
 306 by 0.02. In the following, for any given system clay platelet orientation is characterised by a  
 307 single order parameter, calculated as the mean  $\langle P_2 \rangle$  value for the two methods. Error bars  $\Delta\langle P_2 \rangle$

308 were estimated as the difference between  $\langle P_2 \rangle$  values for the two methods. For the whole series  
 309 of samples,  $\Delta\langle P_2 \rangle$  reached 0.09 at most.



310

311 **Figure. 6** : ODF fitting by eq. (9) from (Dabat et al., 2019) generalized function. Sample: S1  
 312 beidellite + ludox CL-P,  $R_n = 0.3$ . (a) ODF from the first method “azimuthal profile  
 313 subtraction”, fit with eq. (9) and the derived  $\langle P_2 \rangle$  value. (b) ODF from the second method “2D  
 314 SAXS pattern subtraction”, fit with eq. (9) and the derived  $\langle P_2 \rangle$  value. Difference between the  
 315 two methods is  $\Delta\langle P_2 \rangle = 0.02$ .

316

317 3.2 Effect of spheres on clay platelet orientation in self-standing films

318 3.2.1 Small spheres (~30nm)

319 Figure 7 presents the evolution of the order parameter  $\langle P_2 \rangle$  as a function of  $R_n$  for S1  
320 and S3 clay platelets mixed with either positively or negatively charged small spheres.  $\langle P_2 \rangle$  for  
321 films formed purely of platelets are also displayed in Figure 7 and serve as a reference.

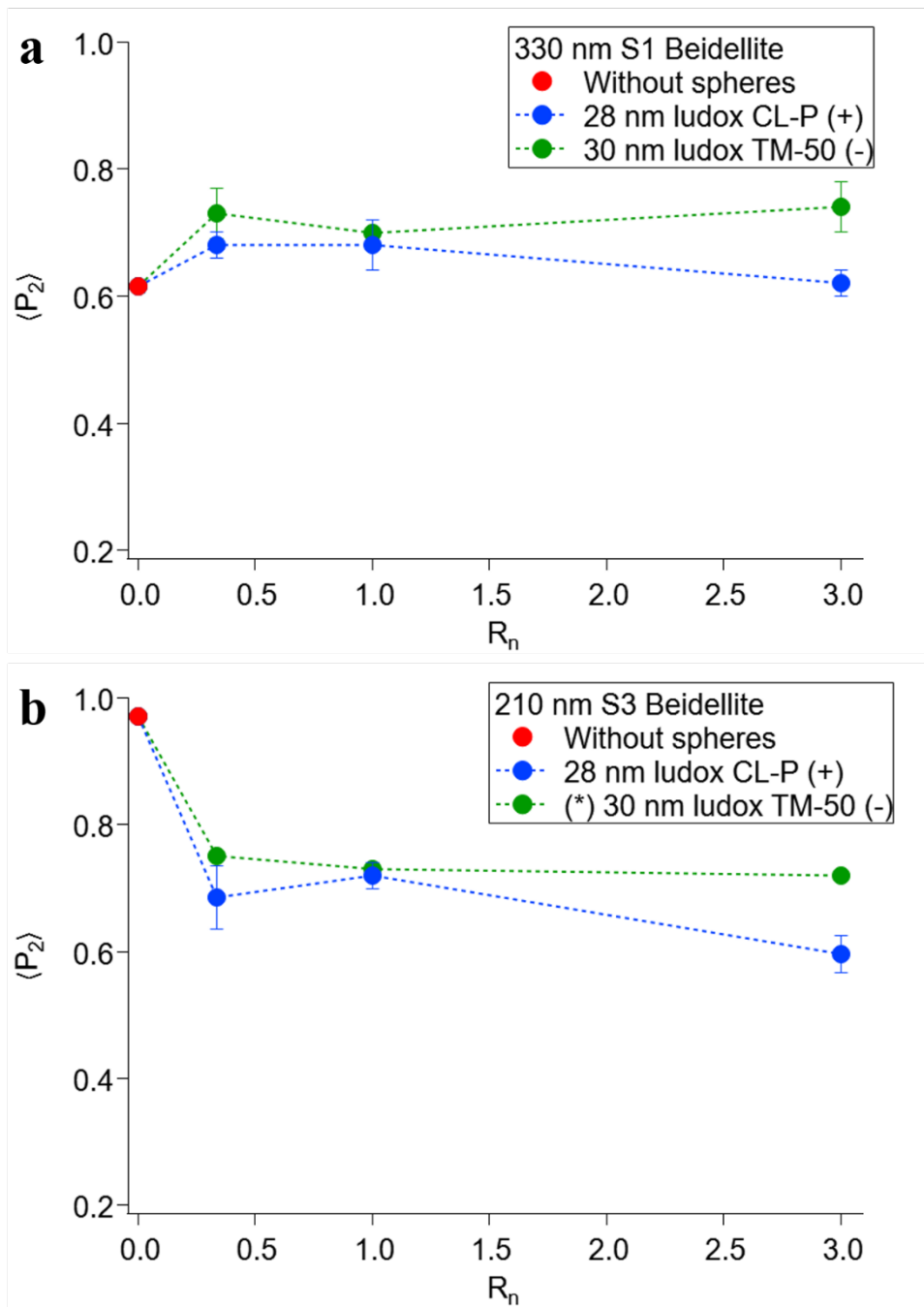
322  $\langle P_2 \rangle$  values for mixed sphere-platelet films, S1 or S3 with positively or negatively  
323 charged spheres, are all similar at the different ratios  $R_n$  (Figure 7). The main difference comes  
324 from the departure structures of clay-only films. Films formed purely of S3 clay platelets exhibit  
325 a very high order parameter, ( $\langle P_2 \rangle = 0.97$ ), in comparison to S1 platelets ( $\langle P_2 \rangle = 0.62$ ) (Figure  
326 7).

327 Upon addition of positively charged ludox CL-P spheres (Figure 7a), the  $\langle P_2 \rangle$  values  
328 for S1 platelets do not display any clear evolution and for the highest ratio spheres/platelets  
329 ( $R_n = 3$ ), the order parameter value is similar to that obtained in the absence of spheres ( $\langle P_2 \rangle =$   
330 0.61). The addition of negatively charged ludox TM-50 spheres appears to lead to a small  
331 increase in  $\langle P_2 \rangle$  that reach values around 0.75.

332 In contrast, adding spheres to S3 beidellite has a significant impact on  $\langle P_2 \rangle$  values  
333 (Figure 7b).<sup>1</sup> The strongly oriented structure of pure S3 beidellite was clearly damaged by both  
334 ludox CL-P and ludox TM-50 spheres (Figure 7b). This is more severe with positively charged  
335 ludox CL-P spheres ( $\langle P_2 \rangle = 0.60$ ) for  $R_n = 3$  than for negatively charged ludox TM-50  
336 ( $\langle P_2 \rangle = 0.72$ ) for  $R_n = 3$  (Figure 7b).

---

<sup>1</sup> (\*) Due to experimental constraints, S3 beidellite mixed with ludox TM-50 dispersions were analyzed as films supported on mylar surfaces. In such conditions, due to the parasitic contribution of Mylar to the SAXS patterns, only the first method could be used for determining  $\langle P_2 \rangle$ . Furthermore, numerous data points were lacking on the data curve  $I(\theta)$  because of unfavorable detector position. We then used a slightly different procedure to calculate the ODF. This procedure is described in (Supplementary info 4)



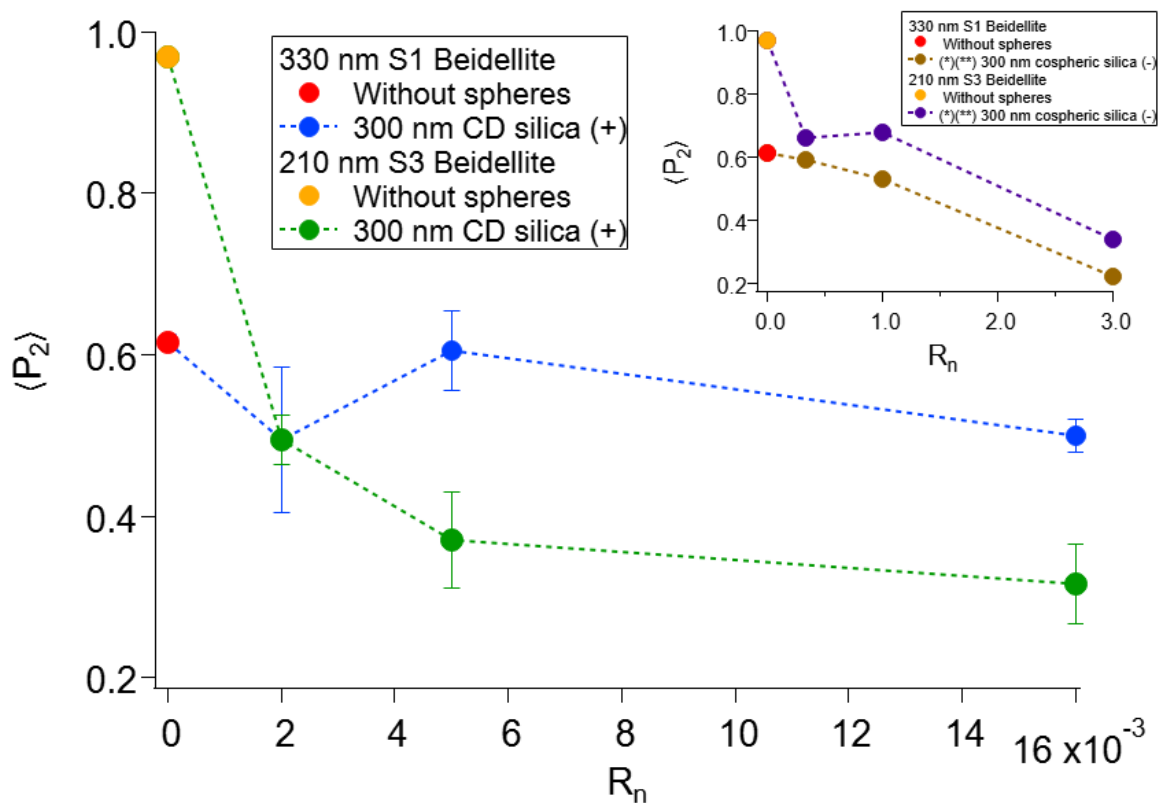
337

338 **Figure. 7** : Evolution of the  $\langle P_2 \rangle$  clay platelet order parameter as a function of sphere/platelet  
 339 number ratio  $R_n$  for small spheres (~30nm). (a) Films of S1 platelets only (●), mixed with  
 340 small positive spheres (●) and small negative spheres (●). (b) Films of S3 platelets only (●),  
 341 mixed with small positive spheres (●) and small negative spheres (●).

### 342 3.2.2 Large spheres (~300nm)

343 Figure 8 presents the evolution of the order parameter  $\langle P_2 \rangle$  as a function of  $R_n$  for S1  
 344 and S3 clay platelets mixed with either positively or negatively charged large spheres.  $\langle P_2 \rangle$  for

345 films formed purely of platelets are also displayed in Figure 8 and serve as a reference. Adding  
 346 positive large spheres to S1 platelets doesn't vary  $\langle P_2 \rangle$  values significantly (Figure 8). However,  
 347 compared to the addition of small spheres, a slight decrease (as opposed to increase) in the order  
 348 parameter is observed. Regarding S3 clay platelets, large positive spheres strongly reduce the  
 349  $\langle P_2 \rangle$  values (Figure 8), from 0.97 to 0.32 at the highest  $R_n$  ratio. Negatively charge spheres  
 350 (prepared as films on a mylar support) have equally a strong destructuring effect that seem to  
 351 happen at higher  $R_n$  ratios, contrary to positive spheres (Figure 8)<sup>2</sup>.



352

353 **Figure. 8** : Evolution of the  $\langle P_2 \rangle$  clay platelet order parameter as a function of sphere/platelet  
 354 number ratio  $R_n$  for large spheres (~300nm). Films of S1/S3 platelets only (●)/(●), S1 platelets  
 355 mixed with large positive spheres (●) and S3 platelets mixed with large positive spheres (●).  
 356 (Sub window graph) Films of S1/S3 platelets only (●)/(●), S1 platelets mixed with large  
 357 negative spheres (●) and S3 platelets mixed with large negative spheres (●).

<sup>2</sup> (\*\*) Negative spheres deposits were produced at the same number ratio  $R_n$  as small spheres, considering they didn't need to be self-standing films on mylar surfaces (Table 3).

358

### 359 3.3 Link between microscopic structure and macroscopic mechanical properties 360 of the self-standing films

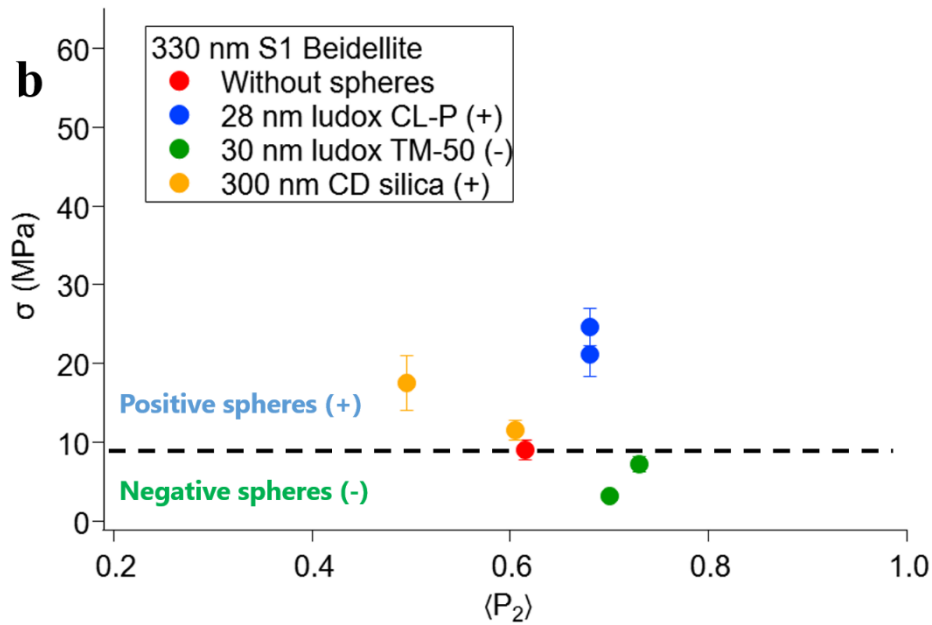
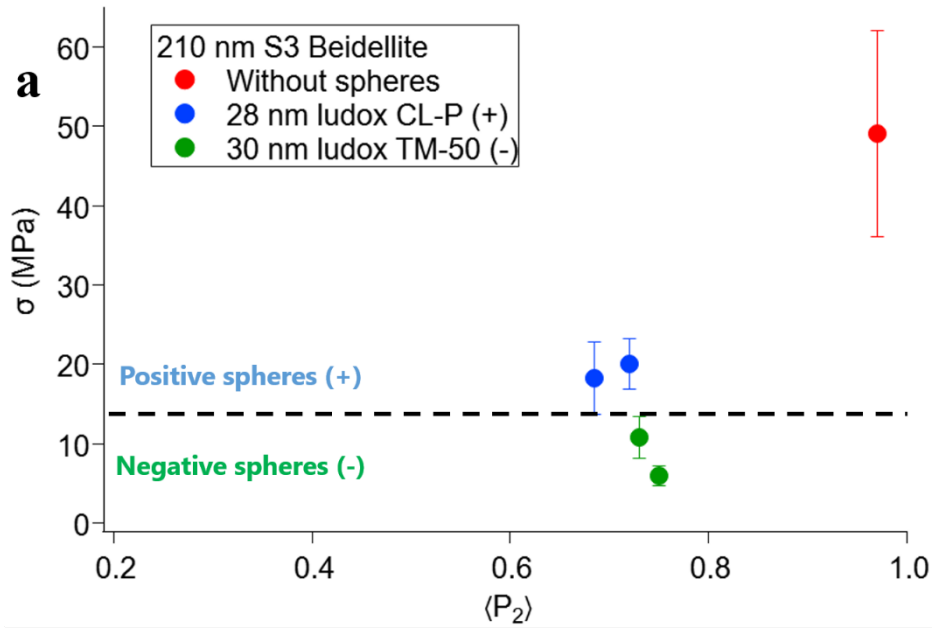
361 The clay nanoplatelet orientation, characterised by the order parameter  $\langle P_2 \rangle$ , describes  
362 a structural feature at the nm-scale. In an attempt to link this microscopic feature to macroscopic  
363 properties of the self-standing films, breaking stress measurements were carried out. Numerous  
364 deposits could not be measured due to their brittleness and this was especially the case for films  
365 with high  $R_n$  ratios and films made of small (S3) platelets and large positive spheres. For brittle  
366 films, it was not possible to cut them into the necessary shape for breaking stress measurements  
367 (Supplementary info 3 and 5). Several trials were made on different films for the same sample,  
368 the number of trials for each sample is summarized in Supplementary info 6. Mean breaking  
369 stress values were determined from the average of the different trials and error bars by  
370 calculating the difference between the higher and lower obtained values. Figure 9 correlates the  
371 breaking stress  $\sigma$  with the order parameter  $\langle P_2 \rangle$  for the entire set of the measured films.

372 Let us consider at first pure clay films. The first point to notice is that the reference system for  
373 small (S3) platelets features a mechanical resistance that stands out as a very strong film among  
374 all the systems studied (Figure 9a). In particular, its breaking stress is significantly higher than  
375 that of the pure film made of large (S1) platelets. We propose that to achieve a mechanically  
376 strong film, two parameters are of importance: (a) the number of stacked platelets inside the  
377 elementary particle (the clay tactoid) and (b) the alignment between adjacent tactoids. It is  
378 possible to evaluate the number of stacked platelets inside tactoids via the width of the 001  
379 stacking peak. According to our measurements (Supplementary info 7), there is no significant  
380 difference in the width of the stacking peak between pure S1 and S3 clay films. Consequently,  
381 the alignment between adjacent tactoids remains the one significant parameter and, indeed, the  
382 pure S3 clay film has a very high  $\langle P_2 \rangle$  values of 0.97. The significantly lower  $\langle P_2 \rangle$  parameter

383 (0.62) for the S1 pure clay film could be ascribed to flexibility of the larger platelets and/or to  
384 size dependent differences in the deposition process itself, as previously reported for  
385 vermiculite clays (Hubert et al., 2013; Ferrage et al., 2015).

386 The importance of the  $\langle P_2 \rangle$  parameter for the mechanical resistance of the films is further  
387 demonstrated by considering the set of S3 films (Figure 9a), for which the addition of both  
388 positively and negatively charged spheres leads to a strong decrease  $\langle P_2 \rangle$ , leading to a drastic  
389 drop of the mechanical breaking stress. For the set of S1 films, with positively and negatively  
390 charged spheres, the picture is not as clear cut: variation of  $\langle P_2 \rangle$  and breaking stress are not as  
391 intense (Figure 9b). However, we can distinguish between the effect of positively and  
392 negatively charge spheres, the former leading to an increase in the breaking stress, the latter to  
393 a decrease of the breaking stress, while all films maintain an intermediate  $\langle P_2 \rangle$  value. Thus,  
394 alignment of adjacent clay tactoids is of the same order for all systems, but attractive  
395 interactions between clays and the added nanospheres may strengthen the contacts between  
396 individual clay tactoids, leading to an enhanced mechanical strength of the film on the  
397 macroscopic scale. The influence of attractive interactions can also be inferred from the S3  
398 systems (Figure 9a). Indeed, films with positively charged spheres also show higher mechanical  
399 strength than films with negatively charged spheres.





400

401 **Figure. 9** : Correlating breaking stress measurements,  $\sigma$ , and clay nanoplatelet orientation, as  
 402 characterised by the order parameter  $\langle P_2 \rangle$  determined by SAXS. Mixed sphere/platelet deposits  
 403 at different  $R_n$  ratio for self-standing films form of (a) large (S1) platelets and (b) small (S3)  
 404 platelets.

405 Here we have not considered neither the influence of the interlayer cation nor the role  
 406 of relative humidity. The impact of these two parameters on the mechanical resistance was  
 407 studied by (Carrier et al., 2016) on montmorillonite films. Effect of interlayer cations on self-

408 standing film morphology, flexibility and gas barrier property was also noted by (Nam et al.,  
409 2009) for montmorillonite. These aspects are directly linked to clay swellability. Exploring  
410 various film formation methods is another perspective, as there are different methods to produce  
411 self-standing films (Zhou et al., 2011).

412

## 413 4 Conclusion

414 Clay platelet orientation and mechanical resistance of self-standing films was  
415 investigated in the presence of charged spheres of different sizes and surface charge. A SAXS  
416 setup and two methodologies of analysis were developed to quantify the clay platelet order  
417 parameter  $\langle P_2 \rangle$  inside several series of sphere/platelet films. Results between the two  
418 methodologies were equivalent.

419 For films formed of large (S1) clay platelets, sphere addition causes a minor  
420 modification of the orientation parameter  $\langle P_2 \rangle$ . The exception is the addition of a high  
421 proportion of large spheres leading to a strong decrease of  $\langle P_2 \rangle$ , down to 0.2. However, such  
422 mixtures can no longer form self-standing films. The situation is very different for small (S3)  
423 platelets. The pure (S3) clay system is particularly well-ordered and addition of any type and  
424 amount of spheres leads to a significant destructuring of the platelet organisation.

425 Link between clay platelet orientation at the microscopic scale and macroscopic  
426 mechanical resistance was investigated with breaking stress measurements. The well-ordered  
427 reference film of pure S3 platelets was by far the strongest film, revealing the importance of  
428 degree of orientation for the mechanical properties of the film. Our data suggest that the  
429 correlation between orientation and mechanical strength is particularly pronounced in the  
430 regime of high order parameter  $\langle P_2 \rangle$ . Furthermore, the nature of interparticle interactions  
431 (attractive/repulsive) has also an effect on the mechanics of the film as, for similar order

432 parameters, clay films containing positive spheres (large and small) exhibit a stronger  
433 mechanical resistance than films containing small negative spheres.

434 This work opens various perspectives about clay materials and their deposits within the  
435 ternary diagram: water-clay-silica. Exploring in detail the relationship between mechanical  
436 stress and the order parameter in the high  $\langle P_2 \rangle$  range ( $>0.7$ ) seems particularly relevant,  
437 especially in the context of soil crusting. Furthermore, the validity of the calculation of the order  
438 parameter  $\langle P_2 \rangle$  should be revisited for the case of concentrated systems. Indeed, this order  
439 parameter is usually used for dilute nematic systems at thermodynamic equilibrium. For  
440 systems outside thermodynamic equilibrium and with a specific morphology, such as self-  
441 standing films, the potential role of the film tortuosity at larger scales for the determination of  
442 the order parameter needs to be evaluated.

443

#### 444 Credit author statement

445 SV, LM and NM wrote the manuscript and conducted the investigation. SV, PL, LM,  
446 TB and NM performed experimental work. SV, PL, LM and NM jointly contributed to the  
447 design of the work. PL, LM, PR, OE, TC and NM supervised the work. All the authors  
448 contributed to the manuscript revision and have approved the manuscript.

449

#### 450 Declaration of competing interest

451 The authors declare that they have no known competing financial interests or personal  
452 relationships that could have appeared to influence the work reported in this paper.

## 453 Acknowledgments

454 The results presented here are part of the PhD thesis of SV funded by the CNRS 80prime  
455 program. This research is also part of the Research Joint Laboratory CARMEN  
456 (Characterization of Materials for new Energy) between IFPEN, CNRS, University of  
457 Strasbourg, ENS Lyon, University of Lyon and Sorbonne University, Paris. The authors  
458 acknowledge the SOLEIL synchrotron for awarding the beam time on beamline SWING  
459 through the BAG scheme No. 20201118. The authors thank Sirine El Mousli (Phenix, Sorbonne  
460 University) and Eric Kohler (IFP Energies Nouvelles) for the TEM and SEM images. The  
461 authors are grateful to Matthieu Vandamme (Ecole des Ponts) for the tensile strength setup and  
462 discussions about mechanical characterization, José Gomes and Frédéric Gélébart (Phenix,  
463 Sorbonne University) for the rotating device and the tools to prepare self-standing films. The  
464 authors would also like to thank Eric Ferrage (University of Poitiers) for helpful discussions  
465 about clay orientation and order parameter calculation.

466

## 467 Supplementary data

468 Figure S1 reports the evolution of the zeta potential in function of pH for the silica spheres.

469 Figure S2 displays the self-standing films and the rotating device.

470 Figure S3 displays the tensile strength setup and the self-standing film under stress.

471 Figure S4 reports the methodology to calculate the order parameter for deposits on mylar.

472 Figure S5 displays self-standing films with brittle structure that were not mechanically  
473 characterized.

474 Table S6 summarizes the number of trials for the different samples characterized with the  
475 tensile strength setup.

476 Figure S7 displays the 001 stacking peak of S1 beidellite and S3 beidellite films without spheres  
477 and the width value of the 001 peak for both films.

478

## 479 References

- 480 Attou, F., Bruand, A., Le Bissonnais, Y., 1998. Effect of clay content and silt—clay fabric on  
481 stability of artificial aggregates. *European Journal of Soil Science* 49, 569–577.  
482 <https://doi.org/10.1046/j.1365-2389.1998.4940569.x>
- 483 Bailey, L., Lekkerkerker, H.N.W., Maitland, G.C., 2015. Smectite clay – inorganic nanoparticle  
484 mixed suspensions: phase behaviour and rheology. *Soft Matter* 11, 222–236.  
485 <https://doi.org/10.1039/C4SM01717J>
- 486 Bergaya, F., Theng, B.K.G., Lagaly, G., 2006. *Handbook of Clay Science*. Elsevier.
- 487 Bruand, A., Prost, R., 1988. Analyse minéralogique quantitative d'un échantillon de sol :  
488 utilisation des données concernant la composition chimique de l'échantillon.  
489 *Agronomie* 8, 15–22. <https://doi.org/10.1051/agro:19880102>
- 490 Bruand, A., Prost, R., 1987. Effect of water content on the fabric of a soil material: an  
491 experimental approach. *Journal of Soil Science* 38, 461–472.  
492 <https://doi.org/10.1111/j.1365-2389.1987.tb02281.x>
- 493 Bruand, A., Tessier, D., Baize, D., 1988. Contribution à l'étude des propriétés de rétention en  
494 eau des sols argileux: importance de la prise en compte de l'organisation de la phase  
495 argileuse. 7.
- 496 Carrier, B., Vandamme, M., Pellenq, R.J.-M., Bornert, M., Ferrage, E., Hubert, F., Van Damme,  
497 H., 2016. Effect of Water on Elastic and Creep Properties of Self-Standing Clay Films.  
498 *Langmuir* 32, 1370–1379. <https://doi.org/10.1021/acs.langmuir.5b03431>
- 499 Dabat, T., Hubert, F., Paineau, E., Launois, P., Laforest, C., Grégoire, B., Dazas, B., Tertre, E.,  
500 Delville, A., Ferrage, E., 2019. A general orientation distribution function for clay-rich  
501 media. *Nat Commun* 10, 5456. <https://doi.org/10.1038/s41467-019-13401-0>
- 502 Dabat, T., Porion, P., Hubert, F., Paineau, E., Dazas, B., Grégoire, B., Tertre, E., Delville, A.,  
503 Ferrage, E., 2020. Influence of preferred orientation of clay particles on the diffusion of  
504 water in kaolinite porous media at constant porosity. *Applied Clay Science* 184, 105354.  
505 <https://doi.org/10.1016/j.clay.2019.105354>
- 506 Doshi, N., Cinacchi, G., van Duijneveldt, J.S., Cosgrove, T., Prescott, S.W., Grillo, I., Phipps,  
507 J., Gittins, D.I., 2011. Structure of colloidal sphere–plate mixtures. *J. Phys.: Condens.*  
508 *Matter* 23, 194109. <https://doi.org/10.1088/0953-8984/23/19/194109>
- 509 Ferrage, E., Hubert, F., Tertre, E., Delville, A., Michot, L.J., Levitz, P., 2015. Modeling the  
510 arrangement of particles in natural swelling-clay porous media using three-dimensional  
511 packing of elliptic disks. *Phys. Rev. E* 91, 062210.  
512 <https://doi.org/10.1103/PhysRevE.91.062210>
- 513 Fiès, J.C., Stengel, P., 1984. Relations entre la constitution granulométrique et minéralogique  
514 et les caractéristiques de l'espace poral des sols 10.
- 515 Geoffroy, V., Dazas, B., Ferrage, E., Tertre, E., Boissard, C., Berenguer, F., Michot, L.J., van  
516 Oort, F., Hubert, F., 2022. Soil crusting: new insight from synchrotron 2D- $\mu$ XRD  
517 mapping of clay-particle orientation and mineralogy ». *Geoderma* 2022.

518 Hermans, P.H., Platzek, P., 1939. Das Lichtbrechungsvermögen der Cellulose in Funktion des  
519 Quellungsgrades. *Recueil des Travaux Chimiques des Pays-Bas* 58, 1001–1007.  
520 <https://doi.org/10.1002/recl.19390581112>

521 Hilhorst, J., Meester, V., Groeneveld, E., Dhont, J.K.G., Lekkerkerker, H.N.W., 2014. Structure  
522 and Rheology of Mixed Suspensions of Montmorillonite and Silica Nanoparticles. *J.*  
523 *Phys. Chem. B* 118, 11816–11825. <https://doi.org/10.1021/jp504217m>

524 Housni, S., Abramson, S., Guigner, J.-M., Levitz, P., Michot, L., 2020. Flocculation and  
525 magnetically-assisted sedimentation of size-sorted beidellite platelets mixed with  
526 maghemite nanoparticles. *Nano Research* 13, 3001–3011.  
527 <https://doi.org/10.1007/s12274-020-2964-9>

528 Hubert, F., Bihannic, I., Prêt, D., Tertre, E., Nauleau, B., Pelletier, M., Demé, B., Ferrage, E.,  
529 2013. Investigating the Anisotropic Features of Particle Orientation in Synthetic  
530 Swelling Clay Porous Media. *Clays and Clay Minerals* 61, 397–415.  
531 <https://doi.org/10.1346/CCMN.2013.0610501>

532 Landman, J., Paineau, E., Davidson, P., Bihannic, I., Michot, L.J., Philippe, A.-M., Petukhov,  
533 A.V., Lekkerkerker, H.N.W., 2014. Effects of Added Silica Nanoparticles on the  
534 Nematic Liquid Crystal Phase Formation in Beidellite Suspensions. *J. Phys. Chem. B*  
535 118, 4913–4919. <https://doi.org/10.1021/jp500036v>

536 Michot, L.J., Bihannic, I., Porsch, K., Maddi, S., Baravian, C., Mougél, J., Levitz, P., 2004.  
537 Phase Diagrams of Wyoming Na-Montmorillonite Clay. Influence of Particle  
538 Anisotropy. *Langmuir* 20, 10829–10837. <https://doi.org/10.1021/la0489108>

539 Nam, H.-J., Ebina, T., Mizukami, F., 2009. Formability and properties of self-standing clay  
540 film by montmorillonite with different interlayer cations. *Colloids and Surfaces A:*  
541 *Physicochemical and Engineering Aspects* 346, 158–163.  
542 <https://doi.org/10.1016/j.colsurfa.2009.06.009>

543 Paineau, E., Antonova, K., Baravian, C., Bihannic, I., Davidson, P., Dozov, I., Impéror-Clerc,  
544 M., Levitz, P., Madsen, A., Meneau, F., Michot, L.J., 2009. Liquid-Crystalline Nematic  
545 Phase in Aqueous Suspensions of a Disk-Shaped Natural Beidellite Clay. *J. Phys.*  
546 *Chem. B* 113, 15858–15869. <https://doi.org/10.1021/jp908326y>

547 Paineau, E., Bihannic, I., Baravian, C., Philippe, A.-M., Davidson, P., Levitz, P., Funari, S.S.,  
548 Rochas, C., Michot, L.J., 2011. Aqueous Suspensions of Natural Swelling Clay  
549 Minerals. 1. Structure and Electrostatic Interactions. *Langmuir* 27, 5562–5573.  
550 <https://doi.org/10.1021/la2001255>

551 Rozenbaum, O., Bruand, A., Le Trong, E., 2012. Soil porosity resulting from the assemblage  
552 of silt grains with a clay phase: New perspectives related to utilization of X-ray  
553 synchrotron computed microtomography. *Comptes Rendus Geoscience* 344, 516–525.  
554 <https://doi.org/10.1016/j.crte.2012.09.004>

555 Soil Survey Staff. 1999. Soil taxonomy: A basic system of soil classification for making and  
556 interpreting soil surveys. 2nd edition. Natural Resources Conservation Service. U.S.  
557 Department of Agriculture Handbook 436., 1999.

558 Stoops, G., Jongerius, A., 1975. Proposal for a micromorphological classification of soil  
559 materials. I. A classification of the related distributions of fine and coarse particles.  
560 *Geoderma* 13, 189–199. [https://doi.org/10.1016/0016-7061\(75\)90017-8](https://doi.org/10.1016/0016-7061(75)90017-8)

561 Velde, B., 1992. Clays as minerals, in: Velde, B. (Ed.), *Introduction to Clay Minerals:*  
562 *Chemistry, Origins, Uses and Environmental Significance*. Springer Netherlands,  
563 Dordrecht, pp. 41–100. [https://doi.org/10.1007/978-94-011-2368-6\\_3](https://doi.org/10.1007/978-94-011-2368-6_3)

564 Zhou, C.-H., Shen, Z.-F., Liu, L.-H., Liu, S.-M., 2011. Preparation and functionality of clay-  
565 containing films. *J. Mater. Chem.* 21, 15132. <https://doi.org/10.1039/c1jm11479d>

566